Applied Catalysis B: Environmental 339 (2023) 123151

Contents lists available at ScienceDirect

Applied Catalysis B: Environmental

journal homepage: www.elsevier.com/locate/apcatb

Continuous direct air capture and methanation using combined system of membrane-based CO_2 capture and Ni-Ca based dual functional materials

Lingcong Li [a], Shinta Miyazaki [a], Ziyang Wu [a], Takashi Toyao [a], Roman Selyanchyn [b,c,d], Zen Maeno [e,*], Shigenori Fujikawa [c,d,f,**], Ken-ichi Shimizu [a,f,***]

[a] Institute for Catalysis, Hokkaido University, N-21, W-10, Sapporo 001-0021, Japan
[b] Platform of Inter-/Transdisciplinary Energy Research (Q-PIT), Kyushu University, 744 Moto-oka, Fukuoka 819-0395, Japan
[c] International Institute for Carbon Neutral Energy Research (WPI-I2CNER), Kyushu University, 744 Moto-oka, Fukuoka 819-0395, Japan
[d] Research Center for Negative Emissions Technologies (K-NETs), Kyushu University, 744 Moto-oka, Fukuoka 819-0395, Japan
[e] School of Advanced Engineering, Kogakuin University, 2665–1, Nakano-cho, Hachioji 192-0015, Japan
[f] The Center for Energy Systems Design (CESD), Kyushu University, 744 Moto-oka, Fukuoka 819-0395, Japan

ARTICLE INFO

Keywords:
Membrane-based direct air capture (m-DAC)
CO_2 capture and reduction (CCR)
CO_2 methanation
Dual functional materials (DFMs)

ABSTRACT

Direct CO_2 capture from the air by membranes (membrane-based DAC, m-DAC) is a promising new technique to achieve CO_2 net zero emissions. In addition, a continuous system for CO_2 capture and its reduction by hydrogen using coupled reactors has scarcely been investigated. In this study, a new continuous system consisting of a m-DAC and a methanation process (m-DAC-M) was developed. For methanation, Ni nanoparticles supported on Ca-loaded Al_2O_3 (Ni-Ca/Al_2O_3; 10 wt% Ni and 6 wt% CaO) were utilized as a dual functional material (DFM). The Ni-Ca/Al_2O_3 exhibited high CH_4 productivity and selectivity, good stability over 100 h, and high humidity resistance properties at a low reaction temperature of 350 °C. The catalytic properties of Ni-Ca/Al_2O_3 were elucidated using microscopic and spectroscopic techniques. The characterization results indicated that the CaO species not only served as CO_2 adsorption sites to trap concentrated CO_2 from the m-DAC system but also improved the reducibility of oxidized Ni species in the hydrogenation period, thereby promoting the reduction of surface carbonate species to CH_4.

1. Introduction

To prevent the worst consequences of climate change, the Intergovernmental Panel on Climate Change recommends achieving net-zero emissions of CO_2 by 2050, and a variety of technologies to reduce atmospheric CO_2 concentrations have been developed in the past decades [1–12]. Currently, two economic approaches are mainly considered. One is the removal of CO_2 from the relatively high concentration (>10%) flue gas of post-combustion industrial point sources [13–17], known as conventional CO_2 capture and storage (CCS). The other is direct air capture (DAC), which directly removes ultralow concentrations of CO_2 (~ 400 ppm) from the air [18–30]. Along with conventional CCS technologies, DAC has recently been recognized as an indispensable technology for establishing a carbon-neutral society. Sorbent-based DAC has been considered the most promising strategy [31–34]. Although industrial pilot plants have been demonstrated, they are not cost-effective or energy-efficient. For example, the smallest economically practical size for the complete DAC process is estimated to be approximately 100 kt-CO_2/year in the KOH-CaO system [34]. Membrane-based CO_2 capture is advantageous for small-scale applications. Recently, Fujikawa et al. developed free-standing polysiloxane nanomembranes for ultra-fast and selective CO_2 permeation [35]. They also proposed a new strategy for membrane-based direct air capture (m-DAC) [27]. All CO_2 capture technologies, including the m-DAC process, should be combined with successive processes to manage captured CO_2.

CO_2 capture and utilization are also a promising approach to emission reduction and the valorization of CO_2 [36]. Among the developed

* Corresponding author.
** Corresponding author at: International Institute for Carbon Neutral Energy Research (WPI-I2CNER), Kyushu University, 744 Moto-oka, Fukuoka 819-0395, Japan.
*** Corresponding author at: Institute for Catalysis, Hokkaido University,N-21, W-10, Sapporo 001-0021, Japan.
E-mail addresses: zmaeno@cc.kogakuin.ac.jp (Z. Maeno), fujikawa.shigenori.137@m.kyushu-u.ac.jp (S. Fujikawa), kshimizu@cat.hokudai.ac.jp (K.-i. Shimizu).

https://doi.org/10.1016/j.apcatb.2023.123151
Received 18 May 2023; Received in revised form 31 July 2023; Accepted 3 August 2023
Available online 9 August 2023

technologies, dual functional materials (DFMs) for CO_2 capture and successive reduction to CO/CH_4 (CCR) have been attracting significant attention in the past few years as the most promising technologies. To date, various DFMs consisting of alkali/alkaline earth metal salts for CO_2 capture and catalytically active metals for CO_2 conversion have been developed, and the utilization of exhaust gases containing relatively high concentrations of CO_2 has been suggested [37–49]. Recently, a few studies on CCR to CH_4 from low concentrations of CO_2 (ca. 400 ppm) have been investigated (direct air capture and methanation, DACM) [18–23,28–30]. For example, Farrauto and co-workers studied DACM by using a Ru-Na_2O/Al_2O_3 DFM under both isothermal conditions (320 °C) and temperature swing operations [18,19]. Kuramoto and co-workers showed that Ni-Na/Al_2O_3 DFM can be applied for DACM at a reaction temperature of 450 °C with increased operation pressure [50]. In all these studies, synthetic air was utilized, and to the best of our knowledge, the CCR of CO_2 from real atmospheric air has not yet been performed. In addition, the number of CCR repetitions in these studies was limited to a few cycles. To achieve realistic social deployment, continuous CO_2 capture from atmospheric air and subsequent hydrogenation are important tasks.

Recently, our research group developed Al_2O_3-supported Pt-Na and Ni-Ca materials as effective DFMs for CCR to synthesize CO and CH_4, respectively [51,52]. We devised a continuous operation system consisting of parallel double reactors and timer-controlled 4-way valves that could continuously capture CO_2 from a mixture with O_2 and then convert it to CO or CH_4 with the repetition of a few thousand cycles of CCR operation. However, the application of CCR to dilute CO_2 in the air has not yet been investigated. In this study, our continuous CCR operation system and m-DAC were combined to convert the CO_2 captured from the air to CH_4 (denoted as m-DAC-M hereinafter). For this purpose, Ni-Ca/Al_2O_3 with a loading of 10 wt% Ni and 6 wt% CaO was prepared for continuous m-DAC-M operation at an isothermal temperature of 350 °C, which is comparable to the operation temperature of the reported Ru-Ca-based DFM systems for DACM [18,19]. The optimized Ni-Ca/Al_2O_3 was characterized using X-ray diffraction (XRD), scanning transmission electron microscopy (STEM), energy-dispersive X-ray spectrometry (EDS), temperature-programmed desorption (TPD), temperature-programmed surface reaction (TPSR), X-ray photoelectron spectroscopy (XPS), in situ X-ray absorption spectroscopy (XAS), and operando Fourier-transform infrared (FT-IR).

2. Experimental section

2.1. Materials for CO_2 separation membrane

Poly(sodium 4-styrene sulfonate) (PSS, average Mw ~70,000) was purchased from Sigma-Aldrich. The two-component polydimethylsiloxane (PDMS) kit (Sylgard184) was purchased from Dow Corning (Corning). Glass substrates (10 cm × 10 cm, ASONE, Japan) were used to fabricate thin polymeric membranes by dip-coating. Hexane (a mixture of isomers, ≥ 96% purity) and ethanol were purchased from Wako Pure Chemicals (Osaka, Japan) and used as received. Deionized water (DI, 18.3 MΩ cm^{-1}) was obtained by reverse osmosis, followed by ion exchange and filtration (Millipore, Direct-QTM), and used for substrate washing and solution preparation. Uncoated microporous polyacrylonitrile (PAN) support membranes (molecular weight cut-off (MWCO) ~20 kDa; retention > 95%) were purchased from Sol-Sep BV (Netherlands; type ID: UF 010104).

2.2. Membrane fabrication

The procedure for thin-film PDMS/PAN composite membrane fabrication in this work was performed according to our previous work [35,53], and is schematically depicted in Fig. S1. Prior to membrane fabrication, the glass substrate was cleaned by ultrasonication in DI water. The substrate was then treated with H_2O plasma (Aqua Plasma® AQ-500, SAMCO, Japan; RF power: 20 W; H_2O flowrate: 20 mL min^{-1}; and chamber pressure: 10 Pa) for 3 min. Aqueous PSS solution (10 wt%) was dip-coated on the glass substrate (lifting speed 0.1 mm/sec, SDI micro dip-coater MD-0408-S5) to form a PSS layer with a thickness of ca. 500 nm. The substrate was heated on a hot plate for 5 min at 120 °C for drying. To prepare the PDMS layer, parts A (base) and B (curing agent) of the Sylgard 184 kit were mixed in a 10:1 ratio and then diluted with hexane to obtain a 10 wt% concentration. This solution was used to dip-coat PDMS on a PSS/glass substrate (lifting speed 0.5 mm/sec), followed by heating on a hot plate for PDMS curing (120 °C, 30 min). Under these conditions, the thicknesses of the prepared PDMS layers were in the range of 400–450 nm. After PDMS layer fabrication, the PDMS/PSS/glass assembly was immersed in water to dissolve the sacrificial PSS layer. This process resulted in the release of the free-standing PDMS nanomembrane that floated on the water surface. The membrane was accurately transferred onto a circular PAN porous support (diameter: 50 mm) and dried in a convection oven (50 °C for 2 h). 10 similar membranes were also prepared.

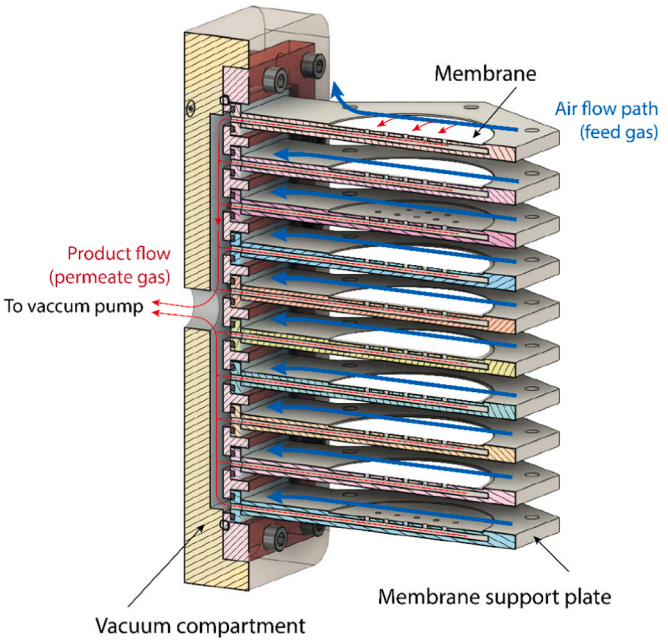

Fig. 1. Schematic structure of the membrane module containing ten plate-supported PDMS/PAN membranes.

2.3. Membrane module fabrication

To compile a larger productivity device, 10 membranes (each with a 10 cm^2 active area) were combined in the plate-and-frame-type homemade module to achieve a total membrane area of 100 cm^2. The module was designed using computer-aided design software (Autodesk, Fusion 360) and printed using an SLA-type 3D printer (Form3, Formlabs). The membrane support plates and vacuum compartment were printed using standard white acrylic resin, whereas the necessary O-ring was printed using Flexible 80 rubbery resin, both obtained from Formlabs. The cross-section of the membrane module device is shown in Fig. 1, demonstrating the gas flow from the feed side to the vacuum side. The necessary connections and fittings were purchased from Swagelok.

2.4. Air separation

For the membrane-based CO_2 separation from atmospheric air (laboratory environment), the permeate side of the designed module was connected to a vacuum pump (Fig. 2). The driving force for gas permeation through the membranes was achieved by vacuuming the

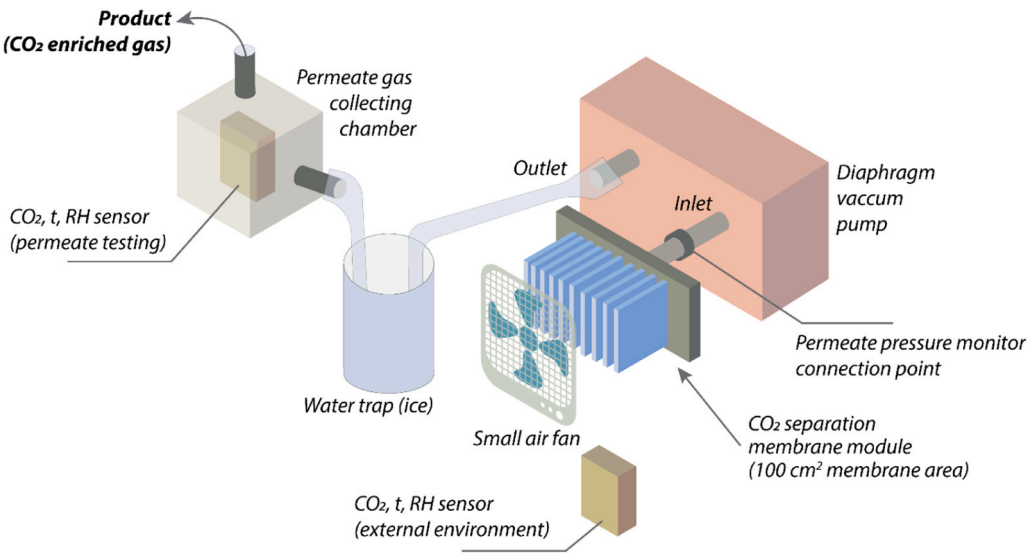

Fig. 2. Schematic of the experimental setup used to achieve the CO_2 preconcentration from the atmospheric air using the m-DAC process.

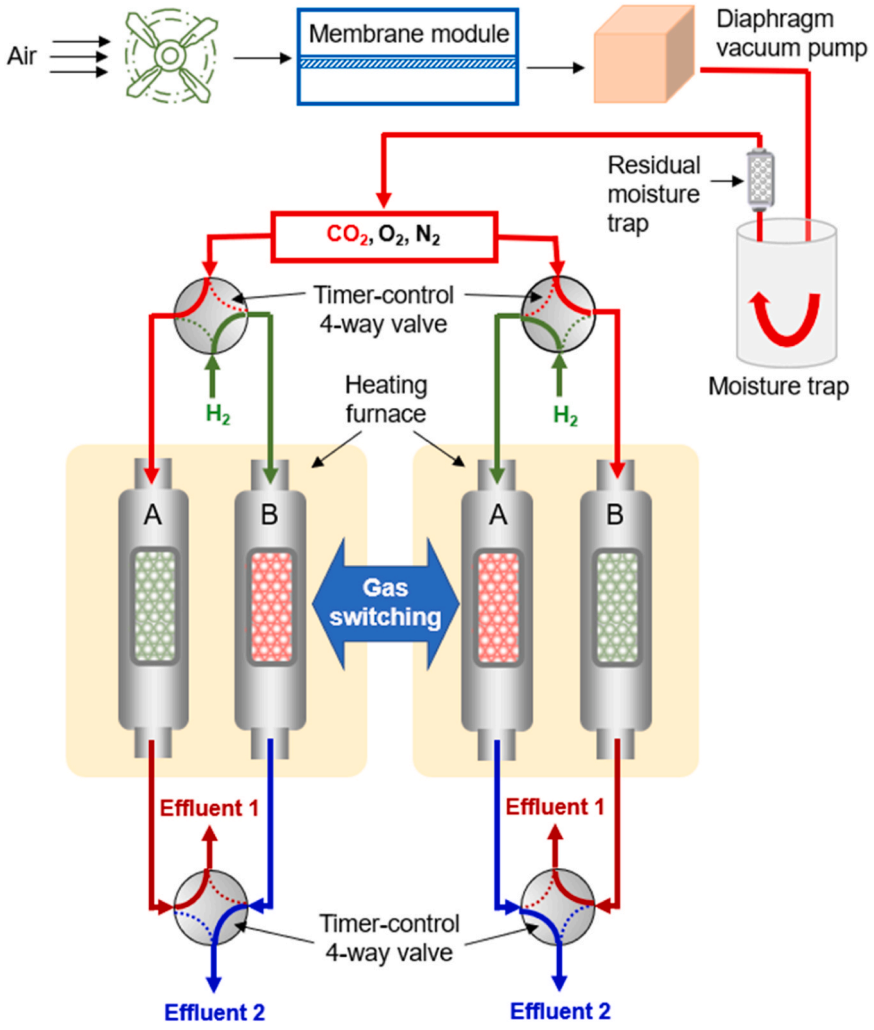

Fig. 3. Schematic of continuous operation m-DAC-M system.

permeate side with the aid of a dry diaphragm pump (DA-41D, ULVAC, Japan), and the permeate pressure was monitored using a capacitance pressure sensor (CCMT-1000D, ULVAC, Japan). Combined sensing logger devices (TR-76Ui-S, T&D Corporation) were used to monitor the CO_2 concentration, temperature, and relative humidity of the gases on both the feed side (atmospheric air) and the permeate side (a box with

Table 1
CO_2 and N_2 permeation properties in the membranes used in this study to fabricate the m-DAC separation module.

Membrane code number	CO_2 permeance, GPU	N_2 permeance, GPU	CO_2/N_2 selectivity
DCM-1	5532	485	11.40
DCM-2	5745	492	11.67
DCM-3	5744	516	11.13
DCM-4	6629	636	10.43
DCM-5	6342	592	10.72
DCM-6	6553	621	10.55
DCM-7	6355	633	10.03
DCM-8	6088	562	10.83
DCM-9	6506	619	10.52
DCM-10	5287	477	11.08

an enclosed sensor connected to the outlet of the vacuum pump). An ice trap was used to remove excess water vapor from the permeate gas.

2.5. Preparation of dual function materials

Dual-functional materials with a 10% Ni active component and 6% CaO adsorber loading were prepared on γ-Al_2O_3 support with an appropriate stoichiometric ratio using the wetness impregnation method. The γ-Al_2O_3 support was obtained by calcination of boehmite (γ-AlOOH, SASOL Chemicals) at 900 °C for 3 h. First, a $Ca(NO_3)_2{\cdot}4\ H_2O$ (AR 98.5%, Fujifilm Wako Pure Chemical Corporation) aqueous solution was added to γ-Al_2O_3 and stirred for 3 h. Afterwards, the Ca-Al_2O_3 mixed suspension was evaporated at 50 °C by using a vacuum pump, followed by drying overnight at 100 °C. The Ca/Al_2O_3 support was obtained after calcination at 600 °C for 2 h. Subsequently, a Ni $(NO_3)_2{\cdot}6\ H_2O$ (AR > 99%, Fujifilm Wako Pure Chemical Corporation) aqueous solution was added to Ca-Al_2O_3. The mixture was stirred at room temperature for 30 min, and then the Ni–Ca/Al_2O_3 suspension was evaporated, dried, and calcined, similar to the Ca-Al_2O_3 support preparation procedure.

2.6. Continuous CO_2 capture from air and utilization through methanation by combined system using m-DAC and Ni-Ca-based DFM

The combined system consisting of an m-DAC and a continuous methanation process is shown in Fig. 3. The membrane module was connected to a vacuum pump, and the outlet of the vacuum pump was connected to the subsequent unit. Before feeding the concentrated CO_2 into the reduction chamber, the stream was first passed through a cold trap, then through a molecular sieve to remove water, and finally passed to the methanation process. The CO_2 concentration in the CO_2 stream or air through the m-DAC was approximately 2000 ppm. The continuously separated fixed-bed flow reactors included two vertical quartz reactors (A and B). 500 mg of Ni-Ca/Al_2O_3 was put on quartz wool in the middle of one of the reactors. Both sides of the reactors were filled with sea sand to decrease the dead volume. Both reactors were placed in an electric tube furnace. Reactors were heated to 450 °C under a N_2 flow at 90 mL min^{-1}, followed by the introduction of 10% H_2/N_2 (100 mL min^{-1}) one by one into the two reactors for pretreatment for 20 min at 450 °C. After the temperature decreased to 350 °C, two timer-controlled 4-way valves were switched on at the same time to continuously collect the effluent gases containing uncaptured CO_2 (effluent 1) and generate CO, CH_4, and desorbed CO_2 (effluent 2) in each outlet line. The compositions of effluents 1 and 2 were monitored using FTIR-1 and FTIR-2 spectroscopy (JASCO FT/IR-4600) equipped with gas cells. The background spectrum was measured after H_2 pretreatment followed by N_2 purging. A CO_2 stream/air was fed to reactor A for 60 s, and then the gas was switched to pure H_2 for 60 s. Conversely, pure H_2 was fed to reactor B for 60 s, and then the gas was switched to the CO_2 stream or air for 60 s. Because the CO_2 concentration and flow rate from the m-DAC

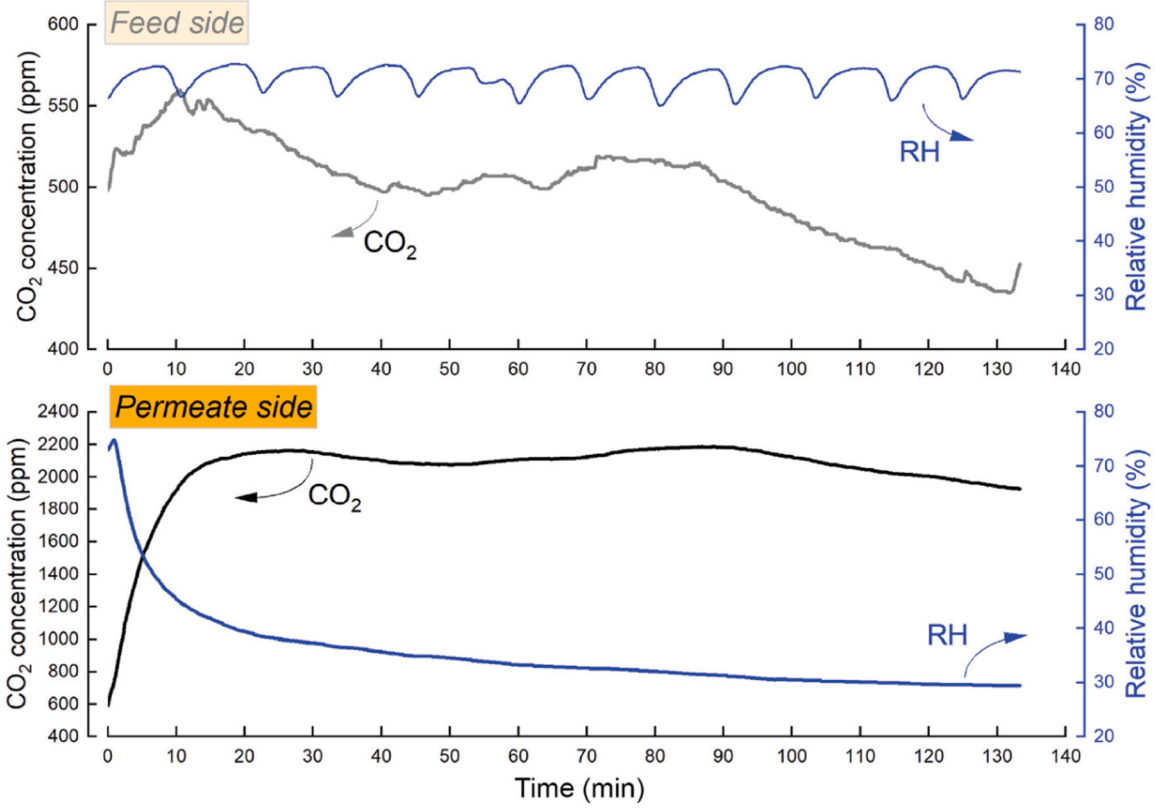

Fig. 4. Typical performance of the m-DAC separation unit enabled to achieve ca. 4.2 times higher CO_2 concentrations in the product gas (permeate side) from atmospheric CO_2 (feed side). After drying, the product gas was used as a feed to the methanation system.

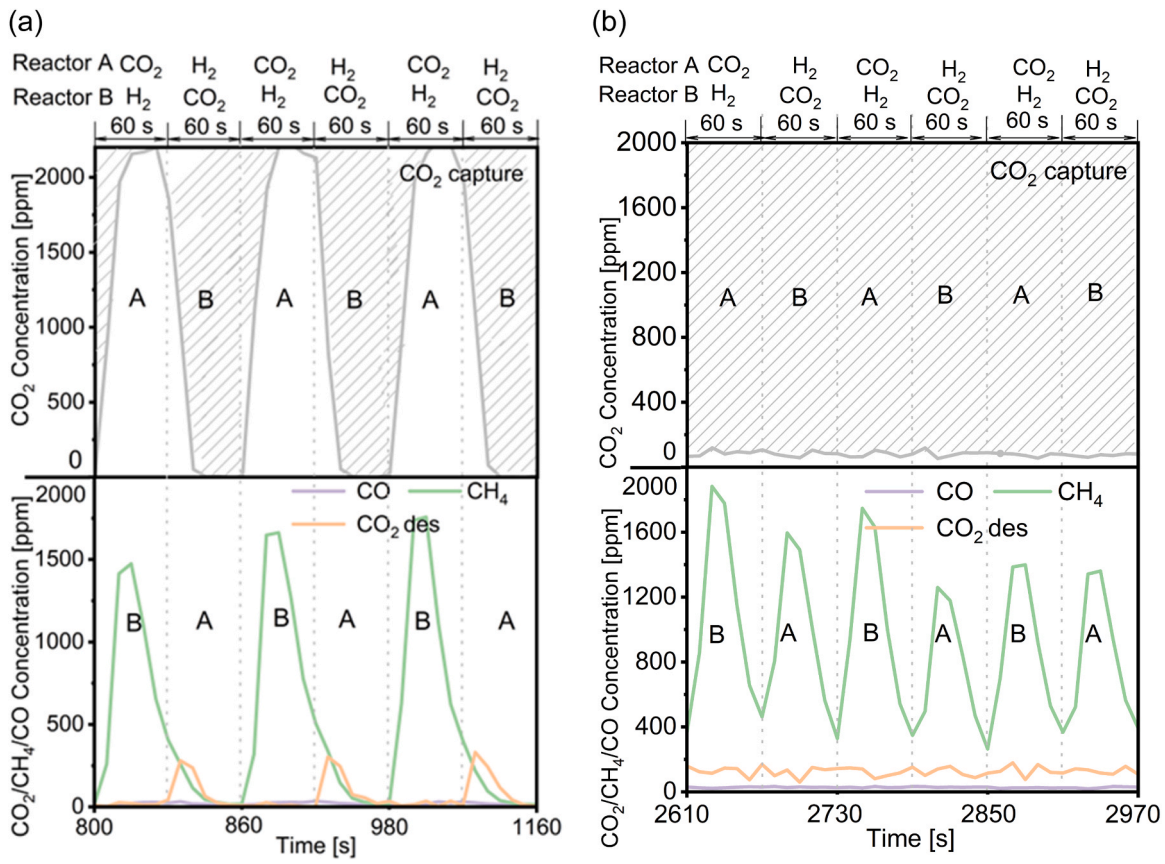

Fig. 5. m-DAC-M over Ni-Ca/Al_2O_3 in (a) single reactor (A: Ni-Ca/Al_2O_3, B: Sea sand) and (b) double reactor (A and B: Ni-Ca/Al_2O_3) systems. Conditions: 500 mg of Ni-Ca/Al_2O_3, the temperature was 350 °C, CO_2 stream/air was allowed to flow for 60 s, followed by a switch to 100 mL min^{-1} of H_2 for 60 s. The concentration of the captured CO_2 fluctuated.

were unstable, the CO_2 adsorption amount and conversion value at this point could not be determined. The normalized CH_4 formation rate was calculated as follows:

$$r_{\cdot CH_4}\ (mmol{\cdot}h^{-1}) = \frac{\int_0^t F_{CH_4}^{out}(t)dt}{t} \quad (1)$$

where $F_{CH_4}^{out}$ is the CH_4 molar flow rate and t stands for the total time for CCR.

3. Results and discussion

3.1. Membrane properties and membrane module performance

Before assembly in the membrane module, each individual membrane was tested for single-gas permeation of CO_2 and N_2. Table 1 summarizes the permeances of each membrane and the ideal membrane CO_2/N_2 selectivity. Considering the additive character of the permeance for each individual membrane when combined in the module (an analog of electric resistance), we estimated that when all membranes were combined in the module device depicted in Fig. 2, it had a CO_2 permeance of 6078 GPU, N_2 permeance of 563 GPU, and CO_2/N_2 selectivity of 10.8. Considering membrane thicknesses of ~ 400–500 nm, these values are close to those of the bulk separation properties of PDMS [35]. Moreover, the consistent selectivity of these membranes proves that membranes do not have physical defects that would allow nonselective gas transport.

Fig. 4 shows the results of the air-separation test conducted in a typical laboratory environment. The results for the feed side showed that the concentration of CO_2 in the atmospheric air varied in the range of 450–550 ppm, and the relative humidity in the room was controlled using an automatic ventilation and air conditioning system, as shown by the wavy curve in Fig. 4 (blue line, feed side). The permeate side showed a much higher concentration of CO_2, which was enabled by the selective transport of gas through the PDMS nanomembranes. After completed gas exchange in the sensing chamber, the system constantly produces gas with ca. 2000–2200 ppm of CO_2 in the product. Although PDMS is also known to have high permeance to water vapor (not assessed in this study), it was removed from the permeate side by passing the vacuum pump outlet (permeate gas) through the ice trap. Therefore, the relative humidity in the chamber was lower than that in the surrounding environment.

3.2. Continuous methanation of concentrated CO_2 by using continuous reactor systems

We compared the m-DAC-M activity using continuous double- and single-reactor systems with Ni-Ca/Al_2O_3 (Fig. 5). In the single reactor system (Fig. 5a), the concentration of uncaptured CO_2 decreased when the CO_2 gas from DAC was flowed in the reactor A. After switching the reactor from A to B for CO_2 flow, the concentration of uncaptured CO_2 increased because the reactor B contains only seas sands (without DFMs). In this period, the hydrogenation of adsorbed CO_2 occurred in the reactor A to give CH_4 where the CH_4 concentration was maximum at 30 s after switching the gas from CO_2 to H_2. The effluent concentration profiles of uncaptured CO_2, generated CH_4 and CO, and desorbed CO_2 during continuous m-DAC-M in a double-reactor system are shown in Fig. 5b. Both the uncaptured and desorbed CO_2 concentrations were approximately 100 ppm at a reaction temperature of 350 °C. The concentration of CO produced was lower than 30 ppm, while the highest concentration of CH_4 formed was approximately 1700 ppm, with a

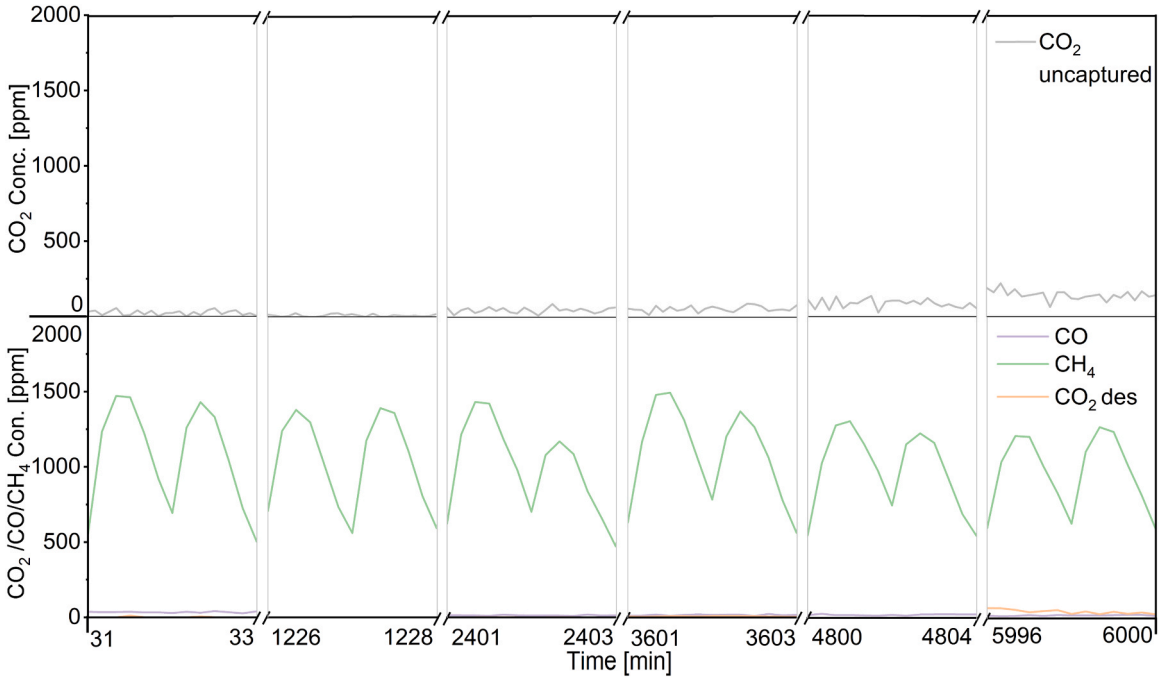

Fig. 6. Long-term m-DAC-M operation over Ni-Ca/Al_2O_3 using double reactors for 100 h. Conditions: 500 mg of Ni-Ca/Al_2O_3 was taken for each reactor; the temperature was 350 °C, CO_2 stream/air was allowed to flow for 60 s, followed by a switch to 60 mL min^{-1} of H_2 for 60 s.

selectivity of 98%. These results demonstrate that the recovered CO_2 was selectively converted to CH_4 with suppressed amounts of uncaptured and desorbed CO_2 as well as generated CO. The CH_4 formation rate using double-reactor system was 225 μmol·h^{-1}, which was higher than that in the single-reactor one (135 μmol·h^{-1}). The short interval time is also requited to obtain efficiently CH_4 because the CH_4 formation mainly occurred within 60 s after switching the gas from CO_2 to H_2 (Fig. S2). Ni/Al_2O_3 and Ca/Al_2O_3 were also studied for m-DAC-M for comparison with Ni-Ca/Al_2O_3 (Fig. S3). When Ni/Al_2O_3 was used in the double reactor system instead of Ni-Ca/Al_2O_3 (Fig. S3a), the concentration of uncaptured CO_2 ranged from 800 to 900 ppm, and the highest concentration of desorbed CO_2 was approximately 200 ppm. Both the CH_4 and CO formation concentrations were much lower than those for Ni-Ca/Al_2O_3. The use of Ca/Al_2O_3 (Fig. S3b) resulted in an uncaptured CO_2 concentration of 400 ppm, a desorbed CO_2 concentration of 240–700 ppm, and almost no CH_4/CO formation. We also used Ni-Ca/Al_2O_3 with a higher CaO loading (30 wt%), which was developed previously in our study [52] for m-DAC-M using a double-reactor system (Fig. S4). Although most of the CO_2 was captured, the concentration of CH_4 formed ranged from 200 to 900 ppm, which is less than that over Ni-Ca/Al_2O_3 with a lower CaO loading (6 wt%). In addition, the CO formation concentration was 200 ppm, which was higher than that of the lower-loading Ni-Ca/Al_2O_3. This indicates that controlling the loading of alkaline (earth) metal oxides is important for promoting m-DAC-M under low-temperature conditions.

The m-DAC process plays an important role in reducing the interval time between CO_2 adsorption and conversion in the DFM. In the DAC step, the m-DAC process concentrates the atmospheric CO_2 concentration (400–500 ppm) to approximately 2000 ppm, and the concentrated air is then introduced into the DFM system. If the air without any enrichment were introduced directly into the DFM system with the same amount of the catalyst, the switching time would be longer to reach the same performance [50]. If a sorbent-based DAC process were used instead of m-DAC, a CO_2 desorption step would be required, significantly reducing the continuity of the process. Therefore, the combination with m-DAC is essential for efficient and continuous conversion.

A long-term continuous m-DAC-M experiment was performed over

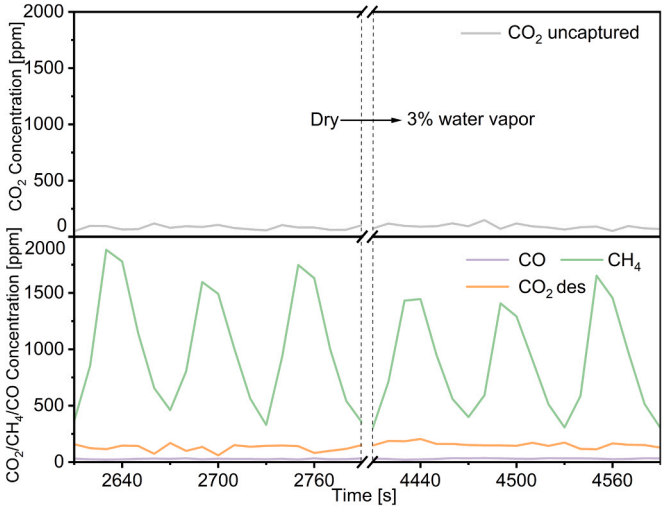

Fig. 7. Operation of m-DAC-M with added water vapor over Ni-Ca/Al_2O_3. Conditions: 0.5 g of Ni-Ca/Al_2O_3 was taken for each reactor; the temperature was 350 °C, CO_2 stream/air with 3% water vapor was allowed to flow for 60 s, followed by a switch to 100 mL min^{-1} of H_2 for 60 s.

100 h on Ni-Ca/Al_2O_3 (Fig. 6). The highest uncaptured and desorbed CO_2 concentrations were stable at 200 and 30 ppm, respectively. The CH_4 formation concentration ranged from 400 ppm to 1700 ppm, and the CO formation concentration was always lower than 30 ppm. The m-DAC-M performance was maintained for at least 100 h, suggesting Ni-Ca/Al_2O_3 has excellent stability at 350 °C. The humidity was considered to simulate a realistic air atmosphere. Water vapor (3%) was introduced into the captured CO_2 stream or air (Fig. 7). The concentrations of captured and desorbed CO_2, as well as the CO formed, were almost the same as the corresponding concentrations under dry conditions. Only the highest concentration of formed CH_4 showed a slight decrease to 1500 ppm. Therefore, the Ni-Ca/Al_2O_3 DFM has the potential to be applied in realistic air atmospheres.

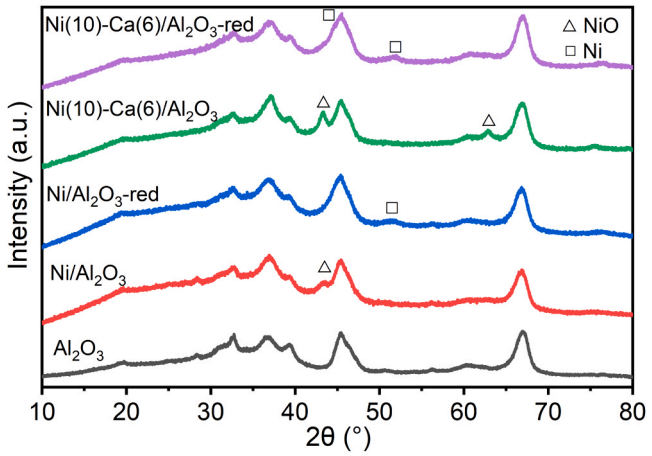

Fig. 8. XRD patterns of calcined and reduced Ni/Al_2O_3 and $Ni\text{-}Ca/Al_2O_3$, and Al_2O_3 support.

3.3. *Influence of co-loaded Ca species on structure and redox property of Ni species*

As described above, we demonstrated a proof of concept to convert atmospheric CO_2 into valuable chemicals or fuels by combining the membrane-based DAC and the CO_2 capture and reductive utilization. In the field of DFMs for CO_2 capture and hydrogenation, the role of basic components, such as Ca species, are recognized as CO_2 capture sites. However, a few studies revealed that basic components affect the structure and chemical property of metal species active for CO_2 hydrogenation, which might result in the different CCR activity. Therefore, in this study, we examined a series of characterization of the present $Ni\text{-}Ca/Al_2O_3$.

The XRD patterns of Al_2O_3, as-calcined Ni/Al_2O_3, $Ni\text{-}Ca/Al_2O_3$, and Ni-loaded materials after H_2 reduction are shown in Fig. 8. Most XRD peaks of Ni/Al_2O_3 and $Ni\text{-}Ca/Al_2O_3$ are consistent with those of γ-Al_2O_3 (JCPDS No. 50–0741), except for the peaks corresponding to NiO (JCPDS No. 47–1049) and/or Ni metal (JCPDS No. 04–0850). Notably, the NiO peaks of $Ni\text{-}Ca/Al_2O_3$ were sharper than those of Ni/Al_2O_3, indicating that NiO crystal growth was promoted on Ca-loaded Al_2O_3. No diffraction peak was observed for the Ca species on $Ni\text{-}Ca/Al_2O_3$, possibly because of the high dispersion of Ca species on the surface of Al_2O_3. Fig. 9 shows the STEM image and EDS mappings of $Ni\text{-}Ca/Al_2O_3$. Ca is highly dispersed on the surface of Al_2O_3. Ni nanoparticles were

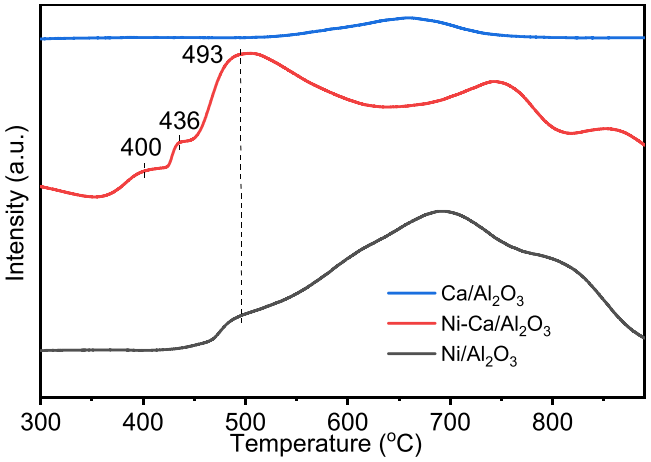

Fig. 10. H_2-TPR profiles of Ni/Al_2O_3, $Ni\text{-}Ca/Al_2O_3$, and Ca/Al_2O_3.

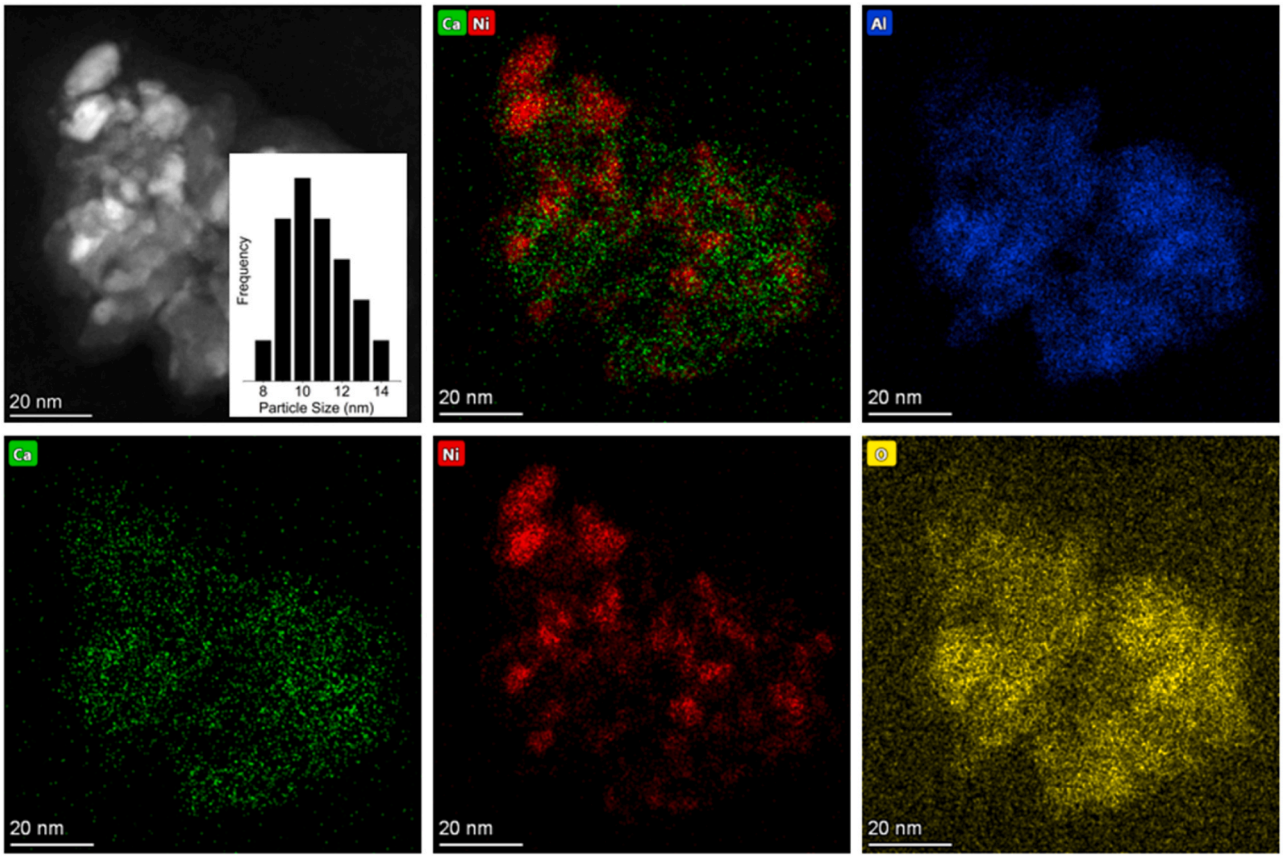

Fig. 9. STEM images and EDS mapping of $Ni\text{-}Ca/Al_2O_3$.

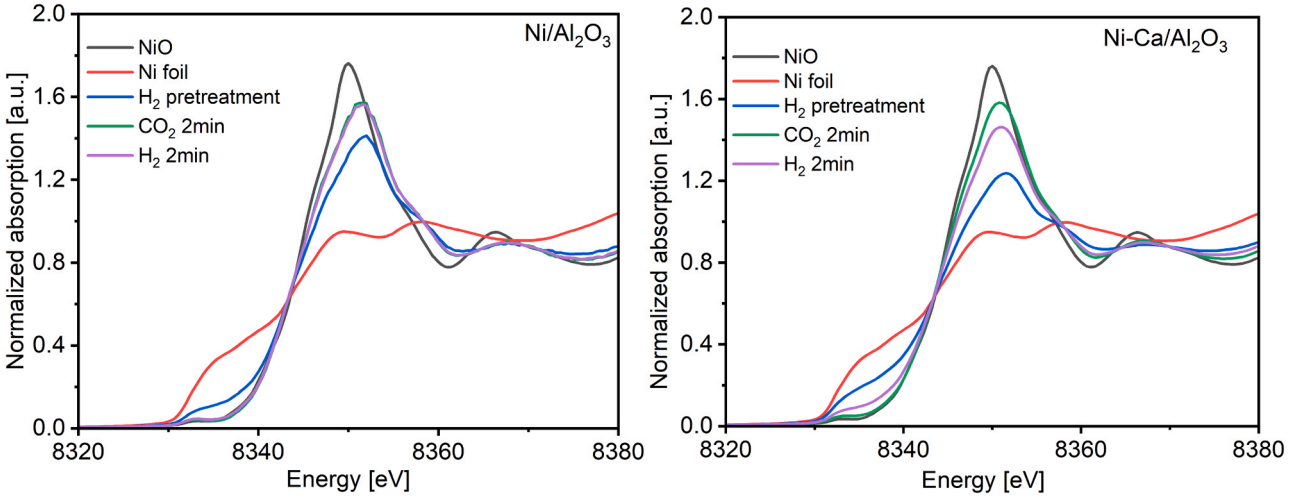

Fig. 11. In situ Ni K-edge XANES spectra of Ni/Al_2O_3 and $Ni\text{-}Ca/Al_2O_3$. Conditions: H_2 pretreatment at 450 °C for 30 min; temperature was reduced to 350 °C; then, 100 mL min^{-1} of 0.5% CO_2/10% O_2/N_2 was allowed to flow in for 2 min, followed by 100 mL min^{-1} of H_2 for 2 min.

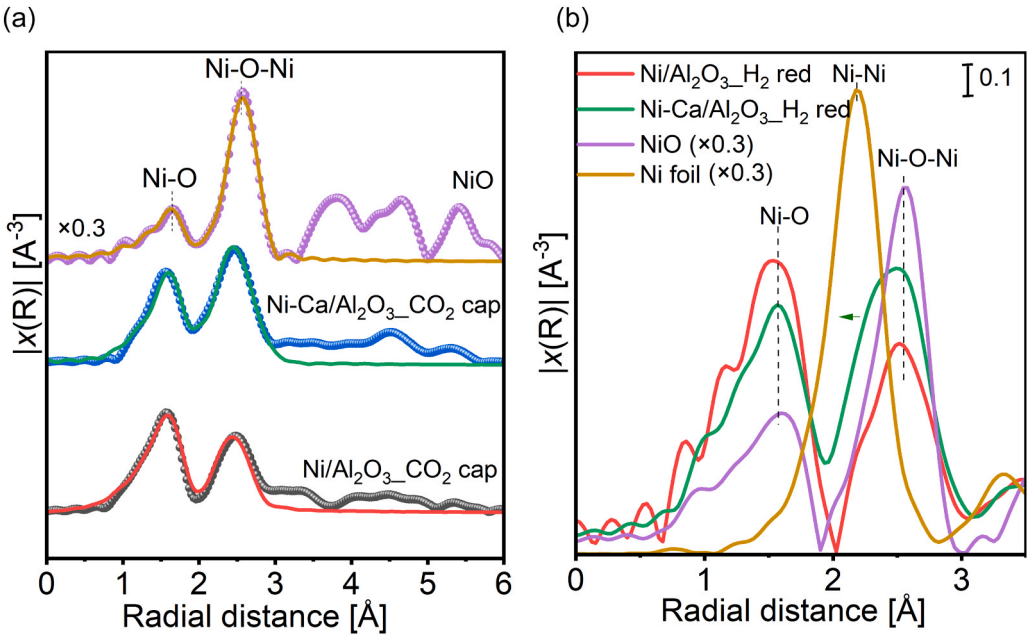

Fig. 12. EXAFS Fourier transforms of Ni/Al_2O_3 and $Ni\text{-}Ca/Al_2O_3$ (CO_2 capture at 350 °C), NiO reference (room temperature), and corresponding fitting curves (a); reduced Ni/Al_2O_3 and $Ni\text{-}Ca/Al_2O_3$ (H_2 reduction at 350 °C), with Ni foil and NiO reference (b).

observed on the Ca-loaded Al_2O_3 surface with an average size of approximately 10 nm, which is larger than the average size of Ni on Ni/Al_2O_3 (7 nm, Fig. S5). These STEM and EDS mapping results are consistent with the XRD results.

Fig. 10 shows the H_2-TPR profiles of $Ni\text{-}Ca/Al_2O_3$ and Ni/Al_2O_3. For Ni/Al_2O_3, the peaks located at 493 °C and higher than 600 °C were ascribed to the reduction of NiO species weakly and strongly interacting with the Al_2O_3 support, respectively [54]. For $Ni\text{-}Ca/Al_2O_3$, two peaks were observed at low temperatures of 400 and 436 °C, which were tentatively assigned to the reduction of strongly adsorbed carbonate species. Moreover, the intensity of the peak at 493 °C on $Ni\text{-}Ca/Al_2O_3$ was stronger than that of Ni/Al_2O_3, indicating that the interaction between NiO and the Al_2O_3 support was weakened by the introduction of the Ca promoter.

The oxidation states of the Ni nanoparticles in Ni/Al_2O_3 and $Ni\text{-}Ca/Al_2O_3$ were investigated using in situ Ni K-edge XANES (Fig. 11). A synthetic CO_2 and O_2 gas mixture was used in this study. First, DFMs were pretreated with H_2 for 30 min at 450 °C. Neither Ni/Al_2O_3 nor $Ni\text{-}Ca/Al_2O_3$ were completely reduced to the Ni metal state (blue lines), but the white-line intensity of $Ni\text{-}Ca/Al_2O_3$ was more close to that of the Ni foil compared to the case of Ni/Al_2O_3. After decreasing the temperature to 350 °C and subsequently introducing 100 mL min^{-1} of 0.5% CO_2/10% O_2/N_2 for 2 min, both Ni species on two DFMs were completely oxidized (green lines) where the white-line intensity was almost same as that of NiO. Next, 100 mL min^{-1} of H_2 was added to the DFMs. For Ni/Al_2O_3, the white-line intensity (purple line) was hardly changed. However, for $Ni\text{-}Ca/Al_2O_3$, the white-line intensity clearly decreased, showing that the Ni species in $Ni\text{-}Ca/Al_2O_3$ was partially reduced at a low reaction temperature of 350 °C with a short interval time. Combined with the results of H_2-TPR, the reducibility of Ni species was enhanced by Ca co-loading on Al_2O_3, resulting in CCR activity of $Ni\text{-}Ca/Al_2O_3$ under relatively low temperature conditions of 350 °C.

Fig. 12a shows the Fourier transforms of the Ni *K*-edge EXAFS spectra for Ni/Al_2O_3 and $Ni\text{-}Ca/Al_2O_3$ after CO_2 capture, the NiO reference, and

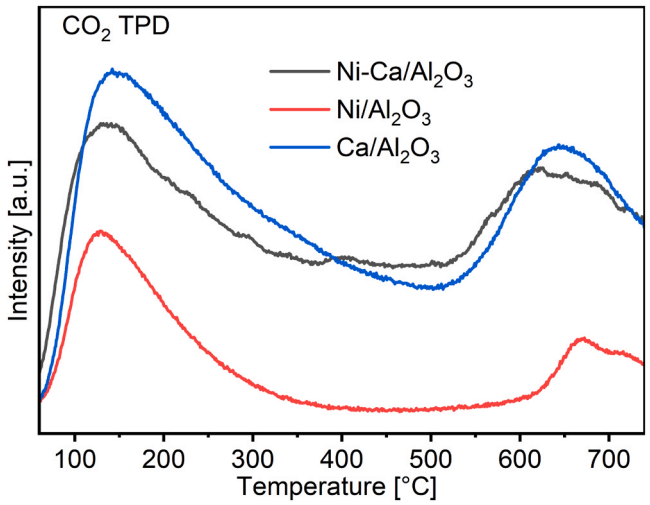

Fig. 13. CO_2 TPD profiles for Ni/Al_2O_3, $Ni\text{-}Ca/Al_2O_3$, and Ca/Al_2O_3. Conditions: 100 mg of DFM, He pretreatment at 500 °C for 30 min, followed by cool down to room temperature and capture of 1%CO_2/He (100 mL min^{-1}); then temperature was increased to 750 °C with pure He (100 mL min^{-1}).

the corresponding curve-fitting results. The peaks around 1.6 and 2.5 Å correspond to the first shell of the NiO phase and the second Ni–Ni shell (Ni–O–Ni bond), respectively. Note that the R-space plots are not phase-corrected and thus do not represent the true bond distances. Both the first Ni–O and second Ni–Ni shell distances on Ni/Al_2O_3 and $Ni\text{-}Ca/Al_2O_3$ are similar to the shell distances of the NiO reference, indicating that these samples have similar bond distances. However, Ni/Al_2O_3 shows a higher peak intensity for the first Ni–O shell than for the second Ni–Ni shell, which is opposite to the peak intensities for the NiO reference. Moreover, according to the fitting results in Table S1, the coordination numbers of the second Ni–Ni shell bond of Ni/Al_2O_3 was determined as 7.4, which is much lower than that of the NiO reference (13.1). This result is possibly caused by the smaller size of NiO on Ni/Al_2O_3 compared to that of the NiO reference. Note that the measurement temperature is different between the DFMs (350 °C) and references (room temperature), which also affects the coordination numbers. For $Ni\text{-}Ca/Al_2O_3$, the peak intensity of the second Ni–Ni shell was higher than that of the first shell of the Ni–O phase, which is the opposite behavior to that of Ni/Al_2O_3. The coordination number of second Ni–Ni shell is 10.9, which is higher than that of Ni/Al_2O_3 (Table S1), supporting the formation of larger Ni nanoparticles in $Ni\text{-}Ca/Al_2O_3$ increased compared to Ni/Al_2O_3.

CO_2 TPD and TPSR measurements were performed to explore their CO_2 desorption and CH_4 formation through the reduction of adsorbed CO_2 with H_2 using $Ni\text{-}Ca/Al_2O_3$, Ni/Al_2O_3, and Ca/Al_2O_3. Fig. 13 shows the CO_2 TPD results. All DFMs showed two obvious CO_2 desorption peaks at 100–200 °C and 600–700 °C, possibly assignable to the weak and strong adsorption of CO_2 onto the surface of Al_2O_3, respectively. In addition, $Ni\text{-}Ca/Al_2O_3$ and Ca/Al_2O_3 showed continuous CO_2 desorption peaks in all temperature ranges, as well as stronger desorption peak intensities than Ni/Al_2O_3, suggesting that CaO on $Ni\text{-}Ca/Al_2O_3$ improved the CO_2 adsorption ability. As for the TPSR profiles of $Ni\text{-}Ca/Al_2O_3$ (Fig. 14), the CO_2 desorption peaks during reduction with H_2 (Fig. 14a) decreased at temperatures higher than 300 °C compared to their corresponding CO_2 TPD peaks. Meanwhile, a large CH_4 formation ($m/z = 16$) peak (Fig. 14b) was observed between 250 and 650 °C for $Ni\text{-}Ca/Al_2O_3$, indicating that the strongly adsorbed CO_2 species were directly converted to CH_4. The CO_2 desorption peaks in the TPSR for Ca/Al_2O_3 and Ni/Al_2O_3 were not significantly different from the TPD peaks (Fig. 13), and only very weak CH_4 formation peaks were detected. This indicates that CO_2 capture and CH_4 formation abilities were significantly improved by Ni loading. In addition, the TPSR experiment was performed using a mixture of CO_2 and O_2 instead of CO_2. The experiment was conducted on a fixed-bed reactor by capturing CO_2 at 30 °C for 10 min and then heating it with H_2 from 30 to 300 °C. CO_2 desorption peaks were detected at 50, 104, and 162 °C, with the CO_2 desorption concentration showing a gradually decreasing tendency (Fig. S6). Conversely, CH_4 formation peaks gradually increased from 129 to 185 °C and maintained high generation concentrations from 180 to 250 °C. This indicates that most of the adsorbed CO_2 was converted to CH_4 at temperatures higher than 180 °C, which is consistent with the TPD and TPSR results.

Operando FTIR measurements during CCR over $Ni\text{-}Ca/Al_2O_3$ were further performed by monitoring the generated gas. Fig. 15a shows the in situ FTIR spectra of the adsorbed carbonate species as a function of temperature. The peak at 1590 cm^{-1} was assigned to bidentate carbonate [55]; the peaks at 1509 and 1390 cm^{-1} were assigned to the monodentate carbonate species on the surface of CaO, respectively [54,

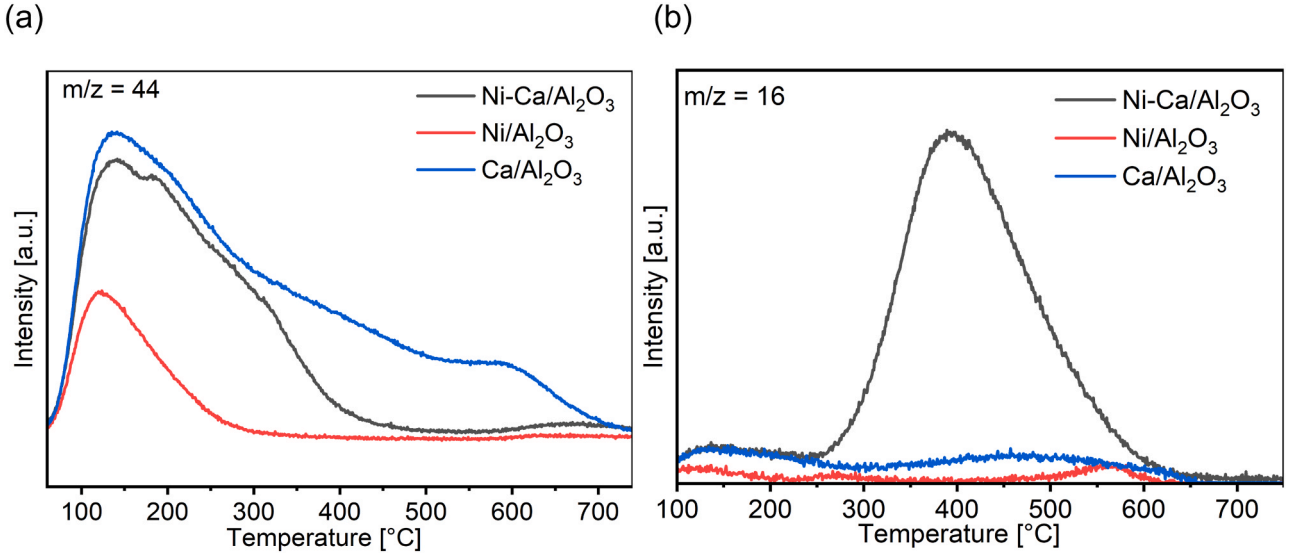

Fig. 14. TPSR profiles of (a) CO_2 desorption and (b) CH_4 formation for Ni/Al_2O_3, $Ni\text{-}Ca/Al_2O_3$, and Ca/Al_2O_3. Conditions: 100 mg of DFM, 10% H_2/He pretreatment at 500 °C for 30 min, followed by cool down to room temperature and capture of 1% CO_2/10% O_2/He (100 mL min^{-1}); then, temperature was increased to 750 °C with 5% H_2/He (100 mL min^{-1}).

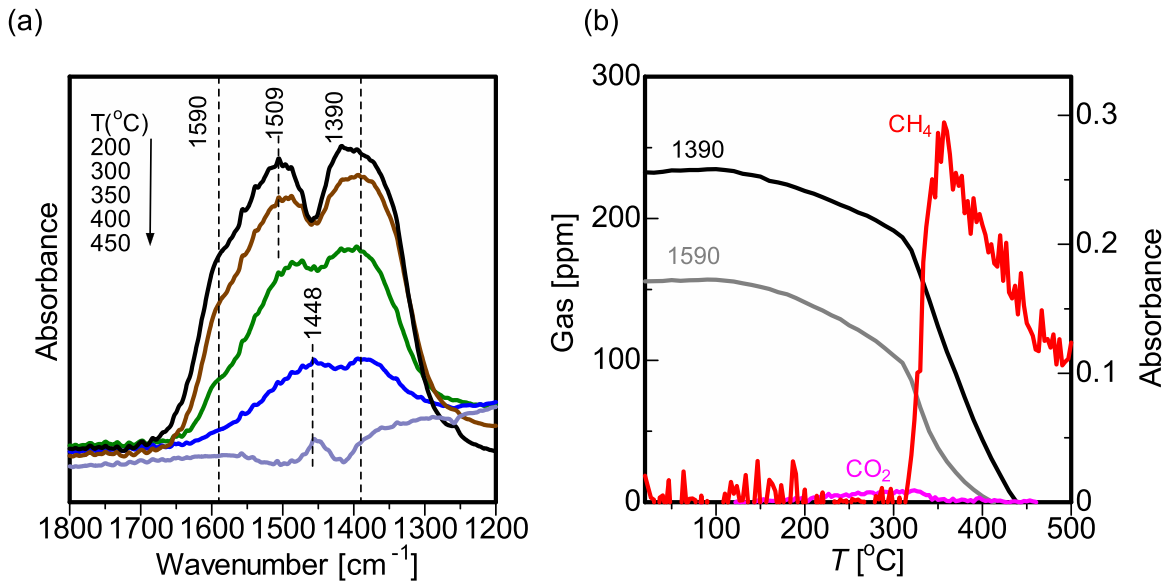

Fig. 15. CO_2-TPSR under H_2 flow for Ni-Ca/Al_2O_3. (a) IR spectra of adsorbed species at different temperatures; (b) IR intensity of carbonates; concentration of desorbed CO_2 and formed CH_4. The background spectra were taken before CO_2 capture. Conditions: after CO_2 capture, 30 mg of catalyst was added for 10 min under 0.5% CO_2/5% O_2/N_2 flow (100 mL min^{-1}) at 25 °C; the flow gas was switched to 10% H_2/N_2 (100 mL min^{-1}); and the temperature was increased from 25 to 500°C.

56]. As the temperature increased, these peaks gradually decreased at temperatures lower than 300 °C and then sharply decreased from 300 to 450°C. Besides, a small peak at 1448 cm^{-1} was detected as the temperature increased to 400 °C, which was attributed to the bulk polydentate carbonates [54,57]. Fig. 15b shows the changes in the kinetic curves of the carbonate species with respect to temperature and CH_4 formation using online gas monitoring. The bidentate and monodentate carbonate species showed a dramatic decrease after the temperature increased to 300 °C, whereas a large CH_4 formation peak was observed at temperatures between 300 and 400 °C. This indicates that the surface carbonate species on Ca species were converted to CH_4 under relatively lower temperature conditions around 350 °C.

The time-resolved operando FTIR spectra were also obtained by fixing the reaction temperature at 350 °C (Fig. S7). Both the bidentate and monodentate carbonates dramatically decreased in the initial 120 s, although some of the monodentate carbonates did not disappear even after 300 s. Meanwhile, a large CH_4 formation peak was detected at approximately 100 s. This further suggests that the desorbed surface carbonates were immediately converted to CH_4. A comparative study was conducted at a reaction temperature of 300 °C using Ni-Ca/Al_2O_3 (Fig. S8). Neither the bidentate nor monodentate carbonate species decomposed completely, even with an extended reaction time of more than 1000 s. Moreover, CH_4 was not formed until the reaction time was more than 500 s. This indicates that 350 °C is a more suitable operating temperature than 300 °C.

4. Conclusion

In this study, a Ni-Ca-based DMF was successfully applied in a new continuous m-DAC-M system for selective methanation at a mild reaction temperature of 350 °C. The concentration of uncaptured CO_2 was less than 100 ppm, and the highest concentration of CH_4 formed was 1700 ppm. A double reactor system was used, and the CO_2 stream or air flow was switched to H_2 at short intervals (60 s). For m-DAC-M, Ni-Ca/Al_2O_3 showed a much higher catalytic activity than Ni/Al_2O_3 and Ca/Al_2O_3. The CO_2 capture capacity and CH_4 productivity were maintained for at least 100 h. In addition, it exhibited good humidity resistance, which is essential for real-world applications. A comprehensive characterization of Ni-Ca/Al_2O_3, Ni/Al_2O_3, and Ca/Al_2O_3 was performed using various microscopic and spectroscopic techniques. Based on the XRD, STEM, and EDS analyses, the Ca species were highly dispersed on Al_2O_3, and nanosized Ni species were formed over the Ca-loaded Al_2O_3. CO_2 capture capacity and CH_4 formation ability were enhanced by Ni co-loading on the Ca-loaded Al_2O_3. The H_2-TPR, XANES, and EXAFS results clarified that NiO in Ni-Ca/Al_2O_3 was more easily reduced than in Ni/Al_2O_3. TPD and TPSR experiments indicated that strongly adsorbed CO_2 species that can be desorbed in the temperature range of 400–650 °C directly underwent hydrogenation, whereas the operando FTIR measurement at an operation temperature of 350 °C indicated that the carbonate species on dispersed CaO were quickly desorbed, and then the desorbed CO_2 was converted to the CH_4 product. CaO species not only serve as CO_2 adsorption sites to trap concentrated CO_2 from m-DAC but also improved the reducibility of the oxidized Ni nanoparticles.

CRediT authorship contribution statement

Lingcong Li: Validation, Investigation, Visualization, Writing – original draft. **Shinta Miyazaki**: Methodology, Investigation. **Ziyang Wu**: Investigation. **Takashi Toyao**: Resources, Writing – review & editing, Funding acquisition. **Roman Selyanchyn:** Methodology, Investigation, Visualization Writing – review & editing, Funding acquisition. **Zen Maeno**: Methodology, Resources, Writing – review & editing, Supervision, Funding acquisition. **Shigenori Fujikawa**: Conceptualization, Writing – review & editing, Supervision, Funding acquisition. **Ken-ichi Shimizu**: Conceptualization, Writing – review & editing, Supervision, Funding acquisition.

Declaration of Competing Interest

The authors declare that they have no known competing financial interests or personal relationships that could have appeared to influence the work reported in this paper.

Data Availability

Data will be made available on request.

Acknowledgements

This study was financially supported by KAKENHI (Grant Nos.

JP20H02775, JP21H04626, and JP22K04806) from the Japan Society for the Promotion of Science (JSPS). This study was also supported by a project, "Moonshot Research and Development Program" (JPNP18016), commissioned by the New Energy and Industrial Technology Development Organization (NEDO) as well as the Joint Usage/Research Center for Catalysis. Z. M. thanks a JACI Prize for Encouraging Young Researcher and the Iwatani Naoji Foundation. L. L. acknowledges a JSPS postdoctoral fellowship (No. P22049). S. M. acknowledges a JST SPRING fellowship (No. JPMJSP2119). EDX measurement was conducted at the Hokkaido University, supported by ″Nanotechnology Platform Program″ of MEXT (Grant No. JPMXP09A21HK0027). The XAS measurements were performed at BL14B2 of SPring-8 (proposal No. 2022A1827).

Appendix A. Supporting information

Supplementary data associated with this article can be found in the online version at doi:10.1016/j.apcatb.2023.123151.

References

[1] G. Singh, J. Lee, A. Karakoti, R. Bahadur, J. Yi, D. Zhao, K. Albahily, A. Vinu, Emerging trends in porous materials for CO_2 capture and conversion, Chem. Soc. Rev. 49 (2020) 4360–4404.
[2] W. Gao, S. Liang, R. Wang, Q. Jiang, Y. Zhang, Q. Zheng, B. Xie, C.Y. Toe, X. Zhu, J. Wang, L. Huang, Y. Gao, Z. Wang, C. Jo, Q. Wang, L. Wang, Y. Liu, B. Louis, J. Scott, A.C. Roger, R. Amal, H. He, S.E. Park, Industrial carbon dioxide capture and utilization: state of the art and future challenges, Chem. Soc. Rev. 49 (2020) 8584–8686.
[3] M. Pera-Titus, Porous inorganic membranes for CO_2 capture: present and prospects, Chem. Rev. 114 (2014) 1413–1492.
[4] M. Ding, R.W. Flaig, H.L. Jiang, O.M. Yaghi, Carbon capture and conversion using metal-organic frameworks and MOF-based materials, Chem. Soc. Rev. 48 (2019) 2783–2828.
[5] G. Cui, J. Wang, S. Zhang, Active chemisorption sites in functionalized ionic liquids for carbon capture, Chem. Soc. Rev. 45 (2016) 4307–4339.
[6] A. Goeppert, M. Czaun, J.P. Jones, G.K. Surya Prakash, G.A. Olah, Recycling of carbon dioxide to methanol and derived products-closing the loop, Chem. Soc. Rev. 43 (2014) 7995–8048.
[7] J.G. Vitillo, B. Smit, L. Gagliardi, Introduction: carbon capture and separation, Chem. Rev. 117 (2017) 9521–9523.
[8] E.S. Sanz-Pérez, C.R. Murdock, S.A. Didas, C.W. Jones, Direct capture of CO_2 from ambient air, Chem. Rev. 116 (2016) 11840–11876.
[9] T.P. Senftle, E.A. Carter, The holy grail: chemistry enabling an economically viable CO_2 capture, utilization, and storage strategy, Acc. Chem. Res. 50 (2017) 472–475.
[10] A.M. Bahmanpour, M. Signorile, O. Kröcher, Recent progress in syngas production via catalytic CO_2 hydrogenation reaction, Appl. Catal. B Environ. 295 (2021), 120319.
[11] S. Sun, S. He, C. Wu, Ni promoted Fe-CaO dual functional materials for calcium chemical dual looping, Chem. Eng. J. 441 (2022), 135752.
[12] S.A. Salaudeen, B. Acharya, A. Dutta, CaO-based CO_2 sorbents: a review on screening, enhancement, cyclic stability, regeneration and kinetics modelling, J. CO_2 Util. 23 (2018) 179–199.
[13] N. Zhang, X. Zhang, Y. Kang, C. Ye, R. Jin, H. Yan, R. Lin, J. Yang, Q. Xu, Y. Wang, Q. Zhang, L. Gu, L. Liu, W. Song, J. Liu, D. Wang, Y. Li, A supported Pd_2 dual-atom site catalyst for efficient electrochemical CO_2 reduction, Angew. Chem. Int. Ed. 60 (2021) 13388–13393.
[14] N. Zhang, X. Zhang, L. Tao, P. Jiang, C. Ye, R. Lin, Z. Huang, A. Li, D. Pang, H. Yan, Y. Wang, P. Xu, S. An, Q. Zhang, L. Liu, S. Du, X. Han, D. Wang, Y. Li, Silver single-atom catalyst for efficient electrochemical CO_2 reduction synthesized from thermal transformation and surface reconstruction, Angew. Chem. Int. Ed. 60 (2021) 6170–6176.
[15] S.B. Jo, J.H. Woo, J.H. Lee, T.Y. Kim, H.I. Kang, S.C. Lee, J.C. Kim, A novel integrated CO_2 capture and direct methanation process using Ni/CaO catal-sorbents, Sustain. Energy Fuels 4 (2020) 4679–4687.
[16] S. Wang, R.J. Farrauto, S. Karp, J.H. Jeon, E.T. Schrunk, Parametric, cyclic aging and characterization studies for CO_2 capture from flue gas and catalytic conversion to synthetic natural gas using a dual functional material (DFM), J. CO_2 Util. 27 (2018) 390–397.
[17] H. Sun, Y. Zhang, S. Guan, J. Huang, C. Wu, Direct and highly selective conversion of captured CO_2 into methane through integrated carbon capture and utilization over dual functional materials, J. CO_2 Util. 38 (2020) 262–272.
[18] C. Jeong-Potter, M. Abdallah, C. Sanderson, M. Goldman, R. Gupta, R. Farrauto, Dual function materials ($Ru+Na_2O/Al_2O_3$) for direct air capture of CO_2 and in situ catalytic methanation: the impact of realistic ambient conditions, Appl. Catal. B Environ. 307 (2022), 120990.
[19] C. Jeong-Potter, R. Farrauto, Feasibility study of combining direct air capture of CO_2 and methanation at isothermal conditions with dual function materials, Appl. Catal. B Environ. 282 (2021), 119416.
[20] M. Fasihi, O. Efimova, C. Breyer, Techno-economic assessment of CO_2 direct air capture plants, J. Clean. Prod. 224 (2019) 957–980.
[21] M.A. Arellano-Treviño, N. Kanani, C.W. Jeong-Potter, R.J. Farrauto, Bimetallic catalysts for CO_2 capture and hydrogenation at simulated flue gas conditions, Chem. Eng. J. 375 (2019), 121953.
[22] A. Bermejo-López, B. Pereda-Ayo, J.A. Onrubia-Calvo, J.A. González-Marcos, J. R. González-Velasco, Tuning basicity of dual function materials widens operation temperature window for efficient CO_2 adsorption and hydrogenation to CH_4, J. CO_2 Util. 58 (2022) 1–11.
[23] J.V. Veselovskaya, A.I. Lysikov, O.V. Netskina, D.V. Kuleshov, A.G. Okunev, K_2CO_3-containing composite sorbents based on thermally modified alumina: synthesis, properties, and potential application in a direct air capture/methanation process, Ind. Eng. Chem. Res. 59 (2020) 7130–7139.
[24] A. Kumar, D.G. Madden, M. Lusi, K.J. Chen, E.A. Daniels, T. Curtin, J.J. Perry, M. J. Zaworotko, Direct air capture of CO_2 by physisorbent materials, Angew. Chem. - Int. Ed. 54 (2015) 14372–14377.
[25] F. Zeman, Reducing the cost of Ca-based direct air capture of CO_2, Environ. Sci. Technol. 48 (2014) 11730–11735.
[26] D.W. Keith, M. Ha-Duong, J.K. Stolaroff, Climate strategy with CO_2 capture from the air, Clim. Change 74 (2006) 17–45.
[27] S. Fujikawa, R. Selyanchyn, T. Kunitake, A new strategy for membrane-based direct air capture, Polym. J. 53 (2021) 111–119.
[28] J.V. Veselovskaya, P.D. Parunin, O.V. Netskina, A.G. Okunev, A novel process for renewable methane production: combining direct air capture by K_2CO_3/alumina sorbent with CO_2 methanation over Ru/alumina catalyst, Top. Catal. 61 (2018) 1528–1536.
[29] D.W. Keith, Why capture CO_2 from the atmosphere? Science 325 (2009) 1654–1655.
[30] C.W. Jones, CO_2 capture from dilute gases as a component of modern global carbon management, Annu. Rev. Chem. Biomol. Eng. 2 (2011) 31–52.
[31] C. Beuttler, L. Charles, J. Wurzbacher, The role of direct air capture in mitigation of anthropogenic greenhouse gas emissions, Front. Clim. 1 (2019) 1–7.
[32] N. McQueen, K.V. Gomes, C. McCormick, K. Blumanthal, M. Pisciotta, J. Wilcox, A review of direct air capture (DAC): scaling up commercial technologies and innovating for the future, Prog. Energy 3 (2021), 032001.
[33] R. Chauvy, L. Dubois, Life cycle and techno-economic assessments of direct air capture processes: an integrated review, Int. J. Energy Res. 46 (2022) 10320–10344.
[34] D.W. Keith, G. Holmes, D.S. Angelo, K. Heidel, A process for capturing CO_2 from the atmosphere, Joule 2 (2018) 1573–1594.
[35] S. Fujikawa, M. Ariyoshi, R. Selyanchyn, T. Kunitake, Ultra-fast, selective CO_2 permeation by free-standing siloxane nanomembranes, Chem. Lett. 48 (2019) 1351–1354.
[36] K.M.K. Yu, I. Curcic, J. Gabriel, S.C.E. Tsang, Recent advances in CO_2 capture and utilization, ChemSusChem 1 (2008) 893–899.
[37] Q. Zheng, R. Farrauto, A. Chau Nguyen, Adsorption and methanation of flue gas CO_2 with dual functional catalytic materials: a parametric study, Ind. Eng. Chem. Res. 55 (2016) 6768–6776.
[38] M.S. Duyar, S. Wang, M.A. Arellano-Trevino, R.J. Farrauto, CO_2 utilization with a novel dual function material (DFM) for capture and catalytic conversion to synthetic natural gas: an update, J. CO_2 Util. 15 (2016) 65–71.
[39] L. Proano, M.A. Arellano-Trevino, R.J. Farrauto, M. Figueredo, C. Jeong-Potter, M. Cobo, Mechanistic assessment of dual function materials, composed of Ru-Ni, Na_2O/Al_2O_3 and Pt-Ni, Na_2O/Al_2O_3, for CO_2 capture and methanation by in-situ DRIFTS, Appl. Surf. Sci. 533 (2020), 147469.
[40] S. Wang, E.T. Schrunk, H. Mahajan, R.J. Farrauto, The role of ruthenium in CO_2 capture and catalytic conversion to fuel by dual function materials (DFM), Catalysts 7 (2017) 88/1–88/13.
[41] H. Sun, J. Wang, J. Zhao, B. Shen, J. Shi, J. Huang, C. Wu, Dual functional catalytic materials of Ni over Ce-modified CaO sorbents for integrated CO_2 capture and conversion, Appl. Catal. B Environ. 244 (2019) 63–75.
[42] M.A. Arellano-Trevino, Z. He, M.C. Libby, R.J. Farrauto, Catalysts and adsorbents for CO_2 capture and conversion with dual function materials: limitations of Ni-containing DFMs for flue gas applications, J. CO_2 Util. 31 (2019) 143–151.
[43] K.H. Chai, L.K. Leong, D.S.-H. Wong, D.-H. Tsai, S. Sethupathi, Effect of CO_2 adsorbents on the Ni-based dual-function materials for CO_2 capturing and in situ methanation, J. Chin. Chem. Soc. 67 (2020) 998–1008.
[44] I.S. Omodolor, H.O. Otor, J.A. Andonegui, B.J. Allen, A.C. Alba-Rubio, Dual-function materials for CO_2 capture and conversion: a review, Ind. Eng. Chem. Res. 59 (2020) 17612–17631.
[45] S. Cimino, R. Russo, L. Lisi, Insights into the cyclic CO_2 capture and catalytic methanation over highly performing Li-Ru/Al_2O_3 dual function materials, Chem. Eng. J. 428 (2022), 131275.
[46] A. Bermejo-Lopez, B. Pereda-Ayo, J.A. Gonzalez-Marcos, J.R. Gonzalez-Velasco, Modeling the CO_2 capture and in situ vonversion to CH_4 on dual function Ru-Na_2CO_3/Al_2O_3 catalyst, J. CO_2 Util. 42 (2020), 101351.
[47] A. Porta, C.G. Visconti, L. Castoldi, R. Matarrese, C. Jeong-Potter, R. Farrauto, L. Lietti, Ru-Ba synergistic effect in dual functioning materials for cyclic CO_2 capture and methanation, Appl. Catal. B Environ. 283 (2021), 119654.
[48] Z. Zhou, N. Sun, B. Wang, Z. Han, S. Cao, D. Hu, T. Zhu, Q. Shen, W. Wei, 2D-layered Ni–MgO–Al_2O_3 nanosheets for integrated capture and methanation of CO_2, ChemSusChem 13 (2020) 360–368.
[49] N. Zhang, C. Ye, H. Yan, L. Li, H. He, D. Wang, Y. Li, Single-atom site catalysts for environmental catalysis, Nano Res. 13 (2020) 3165–3182.
[50] F. Kosaka, Y. Liu, S.Y. Chen, T. Mochizuki, H. Takagi, A. Urakawa, K. Kuramoto, Enhanced activity of integrated CO_2 capture and reduction to CH_4 under

pressurized conditions toward atmospheric CO_2 utilization, ACS Sustain. Chem. Eng. 9 (2021) 3452–3463.
[51] L. Li, S. Miyazaki, S. Yasumura, K.W. Ting, T. Toyao, Z. Maeno, K.I. Shimizu, Continuous CO_2 capture and selective hydrogenation to CO over Na-promoted Pt nanoparticles on Al_2O_3, ACS Catal. 12 (2022) 2639–2650.
[52] L. Li, Z. Wu, S. Miyazaki, T. Toyao, Z. Maeno, K. Shimizu, Continuous CO_2 capture and methanation over Ni-Ca/Al_2O_3 dual functional materials, RSC Adv. 13 (2023) 2213–2219.
[53] O. Selyanchyn, R. Selyanchyn, S. Fujikawa, Critical role of the molecular interface in double-layered pebax-1657/PDMS nanomembranes for highly efficient CO_2/N_2 fast separation, ACS Appl. Mater. Interfaces 12 (2020) 33196–33209.
[54] J. Hu, P. Hongmanorom, V.V. Galvita, Z. Li, S. Kawi, Bifunctional Ni-Ca based material for integrated CO_2 capture and conversion via calcium-looping dry reforming, Appl. Catal. B Environ. 284 (2021), 119734.
[55] A. Quindimil, M.C. Bacariza, J.A. González-Marcos, C. Henriques, J.R. González-Velasco, Enhancing the CO_2 methanation activity of γ-Al_2O_3 supported mono- and bi-metallic catalysts prepared by glycerol assisted impregnation, Appl. Catal. B Environ. 296 (2021), 120322.
[56] F. Prinetto, G. Ghiotti, R. Durand, D. Tichit, Investigation of acid-base properties of catalysts obtained from layered double hydroxides, J. Phys. Chem. B 104 (2000) 11117–11126.
[57] H. Du, C.T. Williams, A.D. Ebner, J.A. Ritter, In situ FTIR spectroscopic analysis of carbonate transformations during adsorption and desorption of CO_2 in K-promoted HTlc, Chem. Mater. 22 (2010) 3519–3526.